Scientific Research Publishing

Open Journal of Physical Chemistry, 2026, 16(4), 81-102
https://www.scirp.org/journal/ojpc
ISSN Online: 2162-1977
ISSN Print: 2162-1969

# Comparative Apparent Shrinkage Patterns of Newtonian and Non-Newtonian Fluids Stored in Geometrically Distinct Vessels

**Idongesit Effiong Ekpo[1*], Gideon Mudiaga Efetobor[2], Ozioma Achugasim[1], Pereware Adowei[1], Ikodia Orji[1]**

[1]Department of Pure and Industrial Chemistry, Faculty of Science, University of Port Harcourt, Port Harcourt, Nigeria
[2]Department of Chemical/Petroleum Technology, School of Science, Laboratory and Technology, University of Port Harcourt, Port Harcourt, Nigeria
Email: *idongesit.ekpo@uniport.edu.ng

**How to cite this paper:** Ekpo, I.E., Efetobor, G.M., Achugasim, O., Adowei, P. and Orji, I. (2026) Comparative Apparent Shrinkage Patterns of Newtonian and Non-Newtonian Fluids Stored in Geometrically Distinct Vessels. *Open Journal of Physical Chemistry*, **16**, 81-102.
https://doi.org/10.4236/ojpc.2026.164007

**Received:** October 9, 2026
**Accepted:** November 23, 2026
**Published:** November 26, 2026

Copyright © 2026 by author(s) and Scientific Research Publishing Inc.
This work is licensed under the Creative Commons Attribution International License (CC BY 4.0).
http://creativecommons.org/licenses/by/4.0/

Open Access

## Abstract

This study compared the apparent shrinkage behaviour of Newtonian and non-Newtonian fluids stored in vessels with different geometries over 7 days: methanol, ethanol, low-weight crude oil (LWC), medium-weight crude oil (MWC), natural gas condensate (NGC), and natural gas liquid (NGL). Wax appearance behaviour was evaluated by differential scanning calorimetry, while flow classification was assessed from steady-shear rheological measurements. Shrinkage patterns were then monitored for seven days in conical, cuboidal, vertical cylindrical, horizontal cylindrical, and spherical vessels. From the investigation, only MWC exhibited a measurable wax appearance temperature at 31.50˚C. On the other hand, no wax-crystallisation onset was detected above 0˚C for methanol, ethanol, LWC, NGC, and NGL within the DSC protocol used. Rheological analysis indicated that methanol, ethanol, LWC, NGC, and NGL behaved as Newtonian fluids over the tested shear-rate range, while MWC showed non-Newtonian shear-thinning behaviour. It was demonstrated that vessel geometry affected volume retention; the conical vessel produced the highest retained volume, the spherical vessel had the lowest retained volume, NGL and NGC showed the most rapid early losses, and MWC showed the smallest overall decline, as measured at a 95% confidence level. These findings indicate that short-term shrinkage is controlled by the combined effects of fluid volatility, rheological behaviour, wax tendency, and vessel geometry. In particular, vessel-dependent headspace development and exposed liquid surface evolution appear to play important roles in modulating apparent storage loss. The study highlights the importance of integrating fluid properties with vessel design when evaluating storage apparent shrinkage behaviour.

**Keywords**

Void Space, Vessel Geometry, Shear Stress, Wax Crystallization, Rheology, Newtonian Fluids, Non-Newtonian Fluids

## 1. Introduction

When the viscosity of a fluid is constant at a given temperature and pressure, regardless of how quickly it is sheared, the fluid is considered a Newtonian fluid. Examples of Newtonian fluids include single-phase fluids with low to medium viscosity, such as water. Water is an example of a Newtonian fluid. Equation (1) shows that the shear stress ($\tau$) for these fluids is directly proportional to their shear rate ($\dot{\gamma}$). Equation (2) shows that shear stress is the force per unit area that is applied parallel to a surface/layer that tries to make it slide. Equation (1) shows the relationship between these quantities for Newtonian fluids, as derived from conservation equations using appropriate boundary conditions [1] [2].

$$\tau = \mu\dot{\gamma} \tag{1}$$

$$\tau = \frac{F}{A} \tag{2}$$

where:

$\tau$ is in Pa or N/m$^2$.

Dynamic viscosity ($\mu$) is in Pa·s or N·s/m$^2$.

Shear rate $\dot{\gamma}$ is in $s^{-1}$.

Tangential or sideways force (F) is in Pa or N/m$^2$.

Area (A) through which the fluid moves is in m$^2$.

While the equation for non-Newtonian fluids may be described by the power-law (Ostwald-de Waele) equation, as shown in Equation (3), the nature of the equation shows that the viscosity relationship is not linear for non-Newtonian fluids, and apparent viscosity depends on the shear rate. Examples of non-Newtonian fluids are blood and polymer solutions [2]-[5].

$$\tau = K\dot{\gamma}^n \tag{3}$$

where:

The consistency index ($K$) is a viscosity-like measure, which sets the "thickness level" of the fluid in the power-law model. It is measured in Pa·s$^n$.

The flow behavior index (n) indicates how viscosity changes with shear rate; it is dimensionless.

It should be noted that:

n < 1 → shear-thinning (apparent viscosity decreases as shear rate increases).

n = 1 → Newtonian behavior ($\mu = K$).

n > 1 → shear-thickening (apparent viscosity increases as the shear rate increases).

Figure 1 displays the shear stress in a fluid between two parallel plates. A side-

ways force is applied to the top plate, causing the oil layer between the plates to shear (fluid layers slide in the direction of the force, as shown by the small arrows). The bottom plate is fixed, and the shear stress in the substance is defined as in Equation (2) [6].

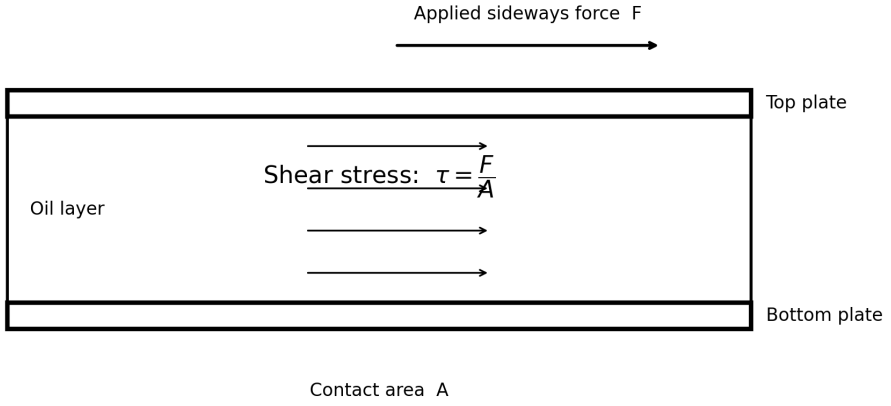


**Figure 1.** Pictorial diagram illustrating the shear stress with a sideways force applied to the top plate over a thin oil layer.

**Figure 2** illustrates simple shear flow between two parallel plates. The bottom plate is stationary (0), while the top plate moves to the right with speed (V). A gap (h) in the direction of the plates separates them. Inside the fluid, the velocity increases from 0 at the bottom plate to (V) at the top plate, as shown by the linear velocity profile v(y). The shear rate is the velocity gradient [6].

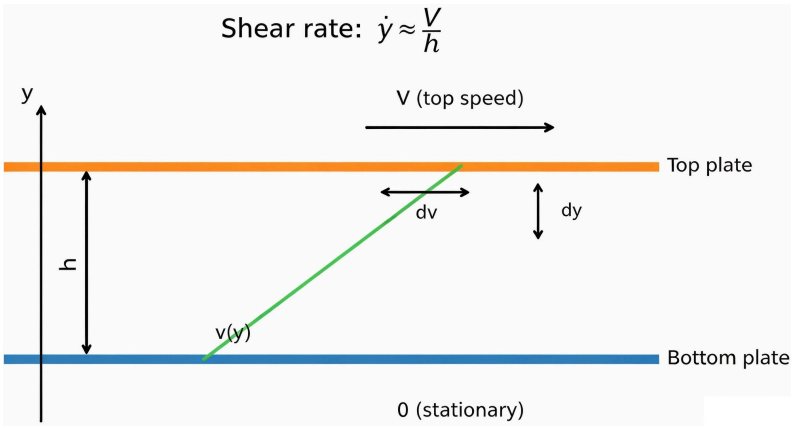


**Figure 2.** Pictorial diagram illustrating the shear rate of fluids with parallel plates separated by a gap h, with the top plate moving at speed V and the bottom plate stationary.

Apparent liquid shrinkage during storage is a persistent source of economic loss, inventory uncertainty, and operational risk in laboratory and field-scale handling of volatile liquids and petroleum stocks [7]-[10].

In this study, shrinkage patterns were monitored over 7 days for 6 fluids stored within the same ambient temperature range (25˚C - 31˚C) in 5 geometrically distinct vessels: vertical cylinder, horizontal cylinder, spherical vessel, conical vessel,

and cuboidal vessel. The fluids comprised ethanol, methanol, natural gas liquid (NGL), natural gas condensate, light crude oil, and medium crude oil [11] [12]. The primary objective was to compare the shrinkage trajectories of upstream and downstream fluids relative to the storage vessel geometry after transfer to the vessels and before discharge from the storage vessel.

## 2. Research Significance

Some causes of volume loss due to shrinkage include evaporation, thermal breathing, wetting, and clingage. Studies have investigated parameters such as vapour pressure, viscosity, API gravity, density, composition, temperature, air movement, humidity, as well as exposed liquid surface area for their contributory effects on shrinkage, but the effects of the Newtonian and non-Newtonian properties of fluids on shrinkage are yet to be fully determined, and comparative side-by-side data linking fluid rheology/wax tendency with vessel geometry and short-term apparent shrinkage are limited; considering these in this discussion is also important because Newtonian and non-Newtonian fluids form the basic substances in upstream and midstream operations. While the role of volatility in storage losses is widely recognized, the combined influence of vessel geometry and fluid rheology is less commonly quantified using side-by-side experimental datasets. In industrial inventory practice, evaporative losses are formalized in standards and guidance documents such as API's Manual of Petroleum Measurement Standards (MPMS) Chapter 19 (evaporation loss measurement), while regulatory emission estimation approaches are summarized in U.S. EPA AP-42, Section 7.1 [13] [14]. Although the present work is laboratory-scaled, the same governing variables, vapor pressure, vapor-space conditions, temperature, and geometry-dependent exposed surface area remain key controls on the interface available for evaporation.

## 3. Materials and Methods

### 3.1. Sample Collection

Materials used for this investigation were upstream natural gas condensate (NGC), light-weight petroleum (LWC), medium-weight crude (MWC), and natural gas liquid (NGL); the four process liquids (NGC, LWC, MWC, NGL) were collected from sample points downstream of a 2-phase vertically cylindrical separator and upstream of the storage facility, at a line pressure of approximately 50 psi. Each sample was a representative composite grab sample at 20 different times within 24 hours, spanning the start-up and end of the transfer operations. Analytical-grade methanol and ethanol, manufactured by Merck KGaA, Darmstadt, Germany, were also used.

### 3.2. Measurement of Shear Stress and Shear Rate (Rheology)

#### 3.2.1. Instrumentation and Measurement Principle

Shear stress ($\tau$) and shear rate ($\dot{\gamma}$) of the six liquid samples (ethanol, methanol, natural gas liquid (NGL), natural gas condensate, light crude oil, and medium

crude oil) were measured using an AMETEK Brookfield RSX rotational rheometer/viscometer. The instrument records torque (M), angular displacement ($\theta$), and angular velocity ($\Omega$). The rheometer software converted these measured signals to shear stress and shear rate using manufacturer-defined geometry factors for the selected measuring system, Equation (4) and (5):

$$\tau = K_{\sigma} M \tag{4}$$

$$\gamma = K_{\gamma} \Omega \tag{5}$$

where $K_{\sigma}$ and $K_{\gamma}$ depend on the geometry type and dimensions.

#### 3.2.2. Temperature Control and Equilibration

Randomized measurements were conducted at 25, 27, 29, 31, and 33 ± 0.01˚C using the rheometer's Peltier temperature control system as the primary temperature-control mechanism. At each set temperature, the loaded sample was allowed to equilibrate for 7 min prior to data acquisition to ensure thermal stability and to reduce thermal drift.

#### 3.2.3. Measuring Geometries (Two-Geometry Protocol)

A two-geometry protocol was adopted based on the expected rheological behaviour of the fluids, as fluid samples had a wide range of viscosities:

Coaxial cylinder (RSX-CC) geometry was used for the low-viscosity fluids (ethanol, methanol, NGL, natural gas condensate, and light crude oil) to enhance measurement stability and minimize free-surface/edge effects.

Parallel-plate geometry was used for the waxy medium crude oil to better capture structured behavior under shear and to allow robust characterization where wall slip may occur. For both geometries, $\tau$ and $\dot{\gamma}$ were computed using the corresponding manufacturer geometry factors.

#### 3.2.4. Instrument Verification

Instrument performance was verified using Cannon viscosity standards (N1000) at 25˚C and 40˚C, with certified viscosities of 2000 cP and 800 cP, respectively, used at the two temperatures, giving instrument readings of 1998 cP and 799 cP, respectively. Verification was performed prior to sample testing under the relevant measurement configuration.

#### 3.2.5. Controlled Shear Rate (CSR) Test Modes and Measurement Programs

In CSR mode, each sample was subjected to a shear-rate sweep from 0.1 to 1000 $s^{-1}$ at each test temperature. The rheometer controlled $\dot{\gamma}$ through angular velocity and geometry factors, measured torque, M, and reported shear stress and apparent viscosity Equation (6):

$$\eta = \frac{\tau}{\dot{\gamma}} \tag{6}$$

Flow curves ($\tau$ vs. $\dot{\gamma}$) and viscosity curves ($\eta$ vs. $\dot{\gamma}$) were recorded.

#### 3.2.6. Controlled Shear Stress (CSS) Test Modes and Measurement Programs

In CSS mode, each sample was subjected to a stress sweep from 0.01 to 7 Pa at each test temperature. The rheometer applied the programmed shear stress (via torque control and geometry factors) and measured the resulting angular velocity response, which was obtained using the manufacturer's geometry factors.

#### 3.2.7. Replication and Data Reporting

Measurements were conducted in triplicate (n = 3) for each sample at each temperature. Mean or standard deviation values were taken from the triplicate values. Rheological behaviour was interpreted using the measured flow curves and viscosity curves, and data were fitted, where appropriate, to Newtonian ( $\tau = \mu\dot{\gamma}$ ) and power-law ( $\tau = K\dot{\gamma}^n$ ) models [15]-[17].

### 3.3. Measurement of Wax Appearance Temperature (WAT)

#### 3.3.1. Principle in WAT Measurement

Wax Appearance Temperature (WAT) is defined here as the onset temperature of wax crystallization detected during controlled cooling of a petroleum liquid using differential scanning calorimetry (DSC); WAT is known for being protocol-dependent and shifts with factors like cooling rate and sample history. As wax crystals begin to form, a crystallization exotherm appears on the DSC heat-flow curve. The WAT is taken as the onset of the first crystallization event, determined using the tangent-intersection (onset) method on the heat-flow baseline and the leading edge of the exotherm.

During the subsequent controlled reheating step, wax crystals melt, producing a melting endotherm. The Wax Disappearance Temperature (WDT) is reported as the onset temperature of this melting endotherm (*i.e.*, the point at which wax crystals are no longer present as the sample transitions back to a single liquid phase) [18]-[20].

#### 3.3.2. Materials and Equipment

Differential Scanning Calorimeter: DSC 3+ (METTLER TOLEDO) with temperature control. The DSC 3+ specification indicates a temperature capability of approximately −150˚C to 700˚C (configuration/cooling-option dependent), confirming that the study's selected window is within the instrument's operational range [21].

Sample pans: Hermetic aluminum DSC pans/lids and a crimping tool (to minimize volatilization and moisture ingress).

Analytical balance (readability ±0.1 mg).

Lint-free wipes, forceps, and tweezers.

Cylinder of nitrogen gas with high purity and flow control.

Samples: ethanol, methanol, natural gas liquids, natural gas condensate, light crude oil, and medium crude oil.

#### 3.3.3. Sample Preparation

(a) Each sample was homogenized prior to weighing to ensure representative

composition (gentle mixing was used to avoid air entrainment).

(b) The sample weighed and introduced into the hermetic aluminum DSC pan was 10.00 ± 0.02 mg, immediately sealed using the crimp tool to limit mass loss from volatilization and to prevent moisture ingress. The same sample mass basis was used for all the samples, and the DSC runs did not create any seal failure.

(c) A matched, sealed empty pan was prepared and used as the reference.

(d) Sealed pans were visually inspected to confirm proper sealing and to ensure that no visible water droplets or large bubbles were present.

#### 3.3.4. Temperature Range and DSC Thermal Program

Temperature window (verified and applied): The experimental program in this study was conducted within 40˚C to −25˚C, selected to bracket the expected wax crystallization/melting events for the samples investigated.

Thermal history erase (melt conditioning): To erase thermal history and promote a uniform initial condition before crystallization, the sample to be analyzed was subjected to 26˚C heat for lower boiling components and 40˚C for higher boiling components and held at an isothermal condition for 20 min.

Cooling scan (WAT determination): The sample was cooled from 20˚C to −25˚C at 2˚C·min$^{-1}$ for lower weight samples and from 40˚C to −25˚C at 2˚C·min$^{-1}$ for higher weight samples.

WAT was recorded as the onset temperature of the first crystallization exotherm using the tangent-intersection onset method.

The crystallization enthalpy (J·g$^{-1}$) was obtained by integrating the exothermic peak area.

#### 3.3.5. Purge Gas and Replication

Stable baseline and reduction of oxidative effects were achieved by a continuous nitrogen purge of 40 - 60 mL·min$^{-1}$, maintained throughout the program. Each sample was analyzed in triplicate [22]-[25].

### 3.4. Storage Vessels and Experimental Design

The storage vessels used in this study were bench-scale vessels intentionally fabricated in multiple geometries to determine the effect of vessel geometry on measured liquid shrinkage.

Even when the vessels were made from small containers with different geometries, the design philosophy was based predominantly on the standards for storage tanks, with an emphasis on integrity, dimensional control, and safe containment of liquids [26].

#### 3.4.1. Design Basis and Sizing Criteria

The storage vessels were produced to withstand a maximum volume of 1.5 ± 0.1 L, which enabled vessels that align with the sufficient liquid volume to withstand repeated volume measurements and ensure comparability of shrinkage trends across geometries under identical ambient conditions. As a global best practice, the required capacity and hold-up volume were considered the primary sizing pa-

rameters before detailing the geometry and fabrication requirements [27].

#### 3.4.2. Structural and Service Considerations

For each geometry, the design was considered:

Hydrostatic loading from the stored liquid column and handling loads (filled and empty conditions).

Self-weight of the vessel and stability during storage measurements.

Containment integrity (leak-tight joints and repeatable closure/cover conditions where applicable).

Seismic actions critical for field tanks were treated in this laboratory-scale fabrication as good-practice design considerations rather than as governing loads due to the laboratory scale [28].

#### 3.4.3. Geometry Development and CAD Modeling

Vessel designs were developed as 2D fabrication drawings and 3D Computer-Aided Design (CAD) models, using Autodesk AutoCAD [29]. CAD modelling was used to (i) standardize dimensions across all vessels, (ii) check geometric consistency prior to fabrication, and (iii) support the layout of cut patterns and assembly drawings.

Five vessels were fabricated strictly according to the CAD drawings to maintain dimensional repeatability across geometries. After fabrication, vessels were checked for dimensional conformity (critical internal dimensions) and capacity conformity to the target range (≈1.5 ± 0.1 L) prior to shrinkage experiments. Also, joints and seams were verified to be leak-tight before use [30] [31].

#### 3.4.4. Rationale for Using a Standards-Aligned Design Language in a Laboratory Study

Although this work is laboratory-scale, storage-tank standards provide a defensible framework for reporting methodology (materials/design/fabrication/inspection mindset). Code-based procedures (e.g., API-type approaches) are often complemented by advanced analyses (e.g., nonlinear dynamic checks) when structural demand increases—supporting the value of standards-anchored reporting even when the application is scaled down.

### 3.5. Tank Volume Measurement to Determine Shrinkage by Innage Gauging

#### 3.5.1. Principle in Tank Volume Measurement

The liquid quantity in each vessel was determined from the measured liquid level (depth) and a vessel-specific calibration chart (capacity table). In manual dipping, a calibrated rule or tape is lowered to a fixed reference (datum), and the wetted line indicates the liquid level; the innage gauge method here could also be referred to as manual dipping. The observed level is then converted to volume using the capacity table prepared for that vessel. This approach follows established manual tank-gauging practice for petroleum and related liquids. The major apparatus used is as follows [30]:

(i) Stainless-steel rule or steel sounding tape calibrated with graduations having a resolution of ≤1 mm.

(ii) Small bob/weight (for tape gauging) to ensure vertical alignment and contact with the datum.

(iii) Oil-indicating paste (gauging paste) to sharpen the liquid contact line and reduce meniscus-reading ambiguity.

(iv) Vessel calibration chart (capacity table) for each geometry, as a function of measured depth, h.

(v) The vessels were designed with equal venting dimensions. The rectangular vent opening is 32 mm × 10 mm, while the circular pipe opening is 23.5 mm in diameter.

#### 3.5.2. Procedure (Bench-Scale Vessels)

Stabilization: After transfer, each vessel was allowed to stand briefly for a period of 5 min to minimize sloshing and to obtain a stable free surface before gauging (important for repeatable level readings). One vessel was filled once and monitored for seven days, with three dip readings each day, giving one (n = 1) independent run per fluid-vessel combination.

Reference-point control: Consistent reference-point control was enhanced as all depth readings were taken to the exact vessel bottom. This was critical because any "zero-offset" between the gauging reference and the calibration table reference introduces a systematic bias in volume results.

Dip preparation: A thin, uniform layer of oil paste was applied to the lower portion of the rule/tape and passed through the 23.5 mm diameter circular pipe opening for manual gauging.

Manual gauging (innage): The measuring tape was lowered vertically until the bob just reached the bottom of the vessel.

The measuring tape was carefully withdrawn, and the measurement of the sharp change in the paste (wetted boundary) was read as the innage depth (h) to the nearest graduation.

Manual gauging steps and key influences (reference point, tape handling, bob effects) are consistent with recognized petroleum manual gauging guidance.

Replicate readings and averaging: The readings were taken in triplicate (without changing the reference point), and the mean depth was recorded as the daily level for that vessel.

Depth-to-volume conversion: Measured depth (h) was converted to volume (V) using the vessel-specific capacity table/calibration chart developed for each geometry. Capacity tables are the standard mechanism for translating gauged levels to contained volumes.

Shrinkage computation: Daily shrinkage, $\Delta V_t$, in Equation (7), the fraction of the change in volume relative to the initial volume, and the daily percentage shrinkage volume, $\%\text{shrinkage}_t$, Equation (8):

$$\Delta V_t = V_0 - V_t \tag{7}$$

$$\%\text{shrinkage}_t = \frac{V_0 - V_t}{V_0} \times 100 \tag{8}$$

### 3.5.3. Vessel Calibration Chart (Capacity Table)

Before shrinkage monitoring, each vessel geometry was calibrated to establish the relationship between measured liquid level ($h$) and contained volume ($V$). Practically, this was done by the stepwise addition of known volumes and recording the corresponding depths to generate a lookup table or fitted function $V = f(h)$. International calibration standards emphasize documenting the calibration method and using the resulting capacity table to determine volume at gauged levels [17] [32].

### 3.5.4. Data Analysis and Comparative Framework

The comparative analysis was organised at two levels: (i) within-fluid ranking of the observed apparent shrinkage across vessel geometries and (ii) comparison of between-fluid retained-volume trajectories over the seven-day storage period, with particular attention to the waxy, non-Newtonian medium crude oil. We interpreted volatility-related losses using established storage-loss concepts involving temperature, pressure, and fluid composition [13], and we considered the rheological behaviour of the waxy crude oil in relation to previous work on wax-structured petroleum systems [23] [33]-[36].

The experimental unit for the storage comparison was the fluid-vessel combination monitored over time. As described in the present experimental record, one storage series was available for each fluid-vessel combination (n = 1 independent storage run per combination). At each scheduled observation, the liquid level was measured three times in the same vessel without changing the gauging reference point (three technical dip readings, n = 3). The three readings were averaged to obtain the representative liquid depth for that observation, which was converted to retained volume using the vessel-specific capacity table. These repeated dips assessed gauging repeatability and did not represent independently prepared or restarted storage runs. We likewise treated successive observations from the same vessel as repeated measurements within one storage series, not as independent replicates.

We therefore summarized retained volume and apparent percentage shrinkage descriptively for each fluid-vessel combination and storage day. Where individual dip readings were available, we used the mean, standard deviation, and range of the three technical readings to describe within-observation measurement repeatability. We reported vessel rankings and differences between fluid trajectories as observed patterns rather than statistically significant effects. Because independent storage replication was not documented, we did not calculate 95% confidence intervals for the mean storage response or perform inferential tests of differences between vessel geometries or fluids; the technical dip readings and successive storage days were not used as substitutes for independent experimental runs.

We evaluated rheological behavior separately from the storage comparison us-

ing the measured shear-stress-shear-rate relationships. Linear and non-linear regression models were fitted, as appropriate, to describe the flow behavior of the liquids, and the coefficient of determination ($R^2$) was used as a descriptive indicator of model fit. Triplicate rheological measurements, where reported, referred to the rheometry protocol and were not counted as independent storage replicates. Accordingly, conclusions about vessel performance and apparent shrinkage were limited to descriptive comparisons under the investigated bench-scale conditions.

#### 3.5.5. Measurement Limitations

We immersed a thermometer and a measurement dipstick in the samples during measurement, which may have caused variation in the measured volume. Using a mass balance to measure the amount of sample retained and a volume-temperature correction factor would have mitigated this limitation.

## 4. Results and Discussion

### 4.1. Waxy Nature of the Investigated Fluids

Table 1 indicates that methanol, ethanol, low-weight crude oil (LWC), natural gas condensate (NGC), and natural gas liquid (NGL) did not show wax crystallization within the DSC temperature window used in this study, and they were treated as wax-free for the temperature range relevant to the shrinkage experiments.

In contrast, the medium-weight crude oil (MWC) showed a clear wax-crystallization onset at 31.50˚C, confirming the presence of precipitable wax components. This implies that, at storage temperatures below (or near) 31.5˚C, MWC is more likely to develop a wax-crystal network that can influence its flow behavior and transport properties, and may therefore contribute to differences in shrinkage and rheological response relative to the wax-free fluids.

Table 1. Wax appearance temperature (˚C) of the investigated fluids.

| Fluid Type | MetOH | EtOH | MWC | LWC | NGC | NGL |
|---|---|---|---|---|---|---|
| WAT (˚C) | ND | ND | 31.50 | ND | ND | ND |

ND—Not detected.

### 4.2. Newtonian and Non-Newtonian Fluids in This Dataset

Figure 3 a-f are steady-shear flow curves (shear stress ($\tau$) plotted against shear rate ($\dot{\gamma}$)). As discussed in the previous sections, a fluid is commonly treated as Newtonian over a tested shear-rate window if $\tau$ increases linearly with $\dot{\gamma}$ and the line passes (approximately) through the origin, implying a constant viscosity ($\mu$) as indicated by the slope [37] [38]. When the curve of shear stress versus shear rate is non-linear or shows an offset intercept (yield stress), the fluid exhibits non-Newtonian behavior (shear-dependent viscosity or yield) [39].

Methanol (a), Ethanol (b), Light crude oil (d), Natural gas condensate (e), and Natural gas liquid (f) each show a straight-line ($\tau - \dot{\gamma}$) trend across the plotted range (0 - 1000 $s^{-1}$), with no pronounced curvature. This indicates that, within the

experimental shear-rate window, their viscosity is effectively shear-independent, so they can be reported as Newtonian fluids under the tested conditions [40].

Medium crude oil (c) shows a clear deviation from linearity: the curve is concave-down (the slope decreases as $\dot{\gamma}$ increases), which is the classic signature of shear-thinning behavior (apparent viscosity decreases with increasing shear rate). This behavior is consistent with waxy crude systems, where wax crystals and microstructural networks can form (especially when tests are conducted below the Wax Appearance Temperature, WAT), producing shear-rate-dependent viscosity and, sometimes, yield stress and time/history effects [41].

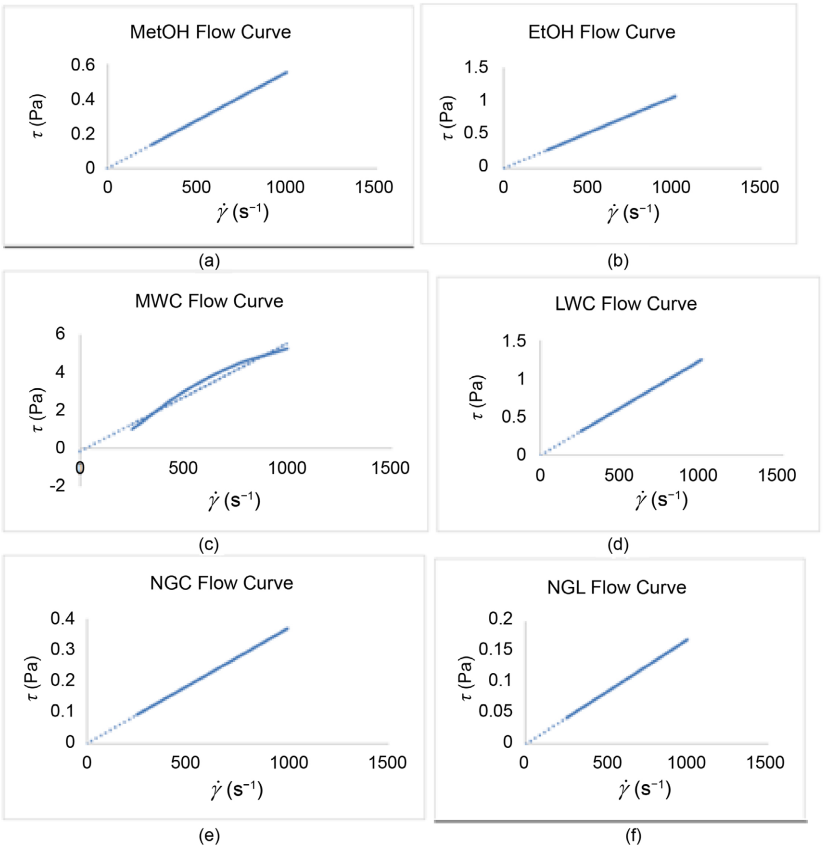


**Figure 3.** Flow curves rheological plots Shear stress ($\tau$) versus Shear rates ($\dot{\gamma}$) of (a) Methanol; (b) Ethanol; (c) Medium molecular weight crude oil (MWC); (d) Low molecular weight crude oil (LWC); (e) Natural gas condensate (NGC); and (f) Natural gas liquid (NGL).

### 4.3. Deduction of Void Spaces in the Storage Vessels' Geometries

Shrinkage due to fluid evaporation in storage systems could be attributed more to the void or internal space not occupied by the fluids. For vessels under atmospheric conditions, vented or imperfectly sealed vessels, headspace is continuously refreshed by ambient air during temperature and pressure swings (breathing), which can enhance evaporative/working losses. The temperature and nature of the volatility of fluids also contribute to interpreting the shrinkage patterns in the

fluids. In addition to these, the rate of mass transfer plays a coordinating role with the liquid-vapor interfacial area and the headspace volume and geometry, as these factors influence vapor accumulation, mixing, and diffusion paths. Particularly, the expansion of void spaces during shrinkage is determined by the storage vessel geometry.

The void spaces across the five (5) vessels at a given time are evaluated as the difference between the total spaces and the liquid spaces at that time; the vessel spaces, here, are referred to as the total liquid-occupied and liquid-unoccupied volumes. The vessel geometries determine their void spaces, as the liquid-vapor interfacial area is important because it influences how quickly vapor is built up and how efficiently it is removed by venting and breathing processes [42] [43].

The conical vessel in **Figure 4(a)** is a right circular cone with a circular base, having a base radius of about 90 mm and an overall height of about 235 mm. For a partially filled cone, the headspace forms a smaller, similar cone above the free surface. As shrinkage lowers the liquid level from the upper (narrow) section toward the lower (wider) section, the free-surface area increases, and the void space expands more rapidly than it would in constant-cross-section vessels, giving an observed variable interfacial area.

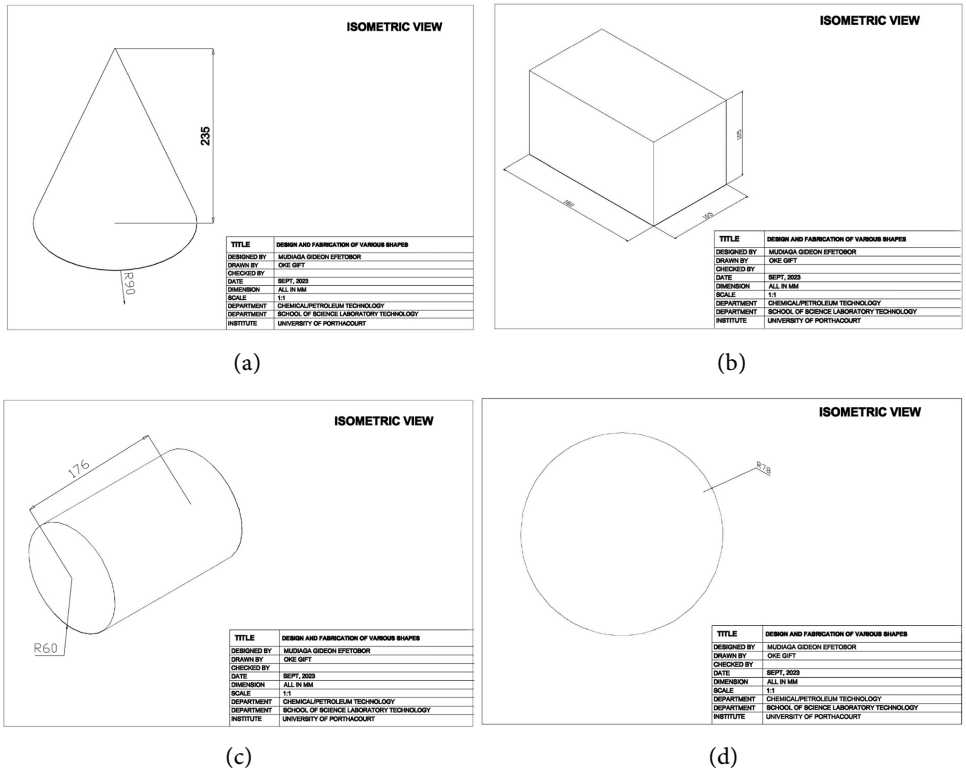


**Figure 4.** Isometric views of storage vessel designs: (a) conical; (b) cuboidal; (c) cylindrical; and (d) spherical.

The cuboidal vessel (**Figure 4(b)**) shows a rectangular prism (cuboid) defined by length (L), breadth (B), and height (H) as shown in the CAD drawing. Here,

the void space is estimated as the rectangular prism above the liquid level, since the cross-sectional area (L × B) is constant with height; both the void volume and the liquid level change approximately linearly as the stored liquid shrinks. It is possible that the constant liquid-vapor interfacial area condition often makes the cuboid a useful baseline geometry for comparing shrinkage trajectories with those of vessels with variable interfacial areas.

The cylindrical vessel in **Figure 4(c)** has a radius of about 60 mm and a length of about 176 mm. In the vertical position, the headspace behaves similarly to the cuboid case, with a constant cross-sectional area ($\pi r^2$), so the void volume at a given time increases linearly as the level falls. In the horizontal position, the void space is a circular-segment volume, and both the measured liquid volume remaining at time (t) and the liquid-vapor interfacial area vary nonlinearly with the fill fraction (due to the changing shape of the liquid cross-section). The orientation-dependent void-space characteristics are important when comparing vertical and horizontal storage configurations in shrinkage studies.

In **Figure 4(d)**, the spherical vessel has an indicated radius of about 78 mm. The headspace is a spherical-cap volume above the free surface. It is observed that the liquid-vapor interfacial area is not constant; it is maximal when the free surface passes near the sphere's equator and decreases as the liquid level moves toward the top or bottom poles. This shows that shrinkage due to evaporation may decrease as the void space decreases; a changing liquid-vapor interfacial area is observed even under identical ambient conditions.

#### Relevance of Void-Space Geometry to Shrinkage Interpretation

The works of [11] and [43] on storage-loss frameworks showed that evaporative and breathing losses depend on liquid volatility and temperature history; venting or breathing frequency; vapor pressure dynamics; the vapor-liquid interface area and headspace conditions that control mass transfer, as well as vapor removal. The experimental data in this study support the use of variation in geometry when comparing or interpreting shrinkages in fluids. Therefore, reporting each vessel's geometry, the expected evolution of void space, and exposed surface area provides the physical basis for linking observed volume-loss trajectories to vessel selection and operational controls.

### 4.4. Geometry-Void-Volume Control of Shrinkage

A view through all six datasets in **Figures 5-10** shows that the shape-dependent ranking of volume retention is consistent with a headspace/void-volume mechanism: vessels that create a smaller effective vapor space above the liquid or a more restricted vapor-air exchange pathway retain more liquid over time, while vessels with a larger vapor space and greater opportunity for vapor renewal show larger apparent shrinkage. According to the investigated storage-loss theory, the dominant drivers of standing ("breathing") and working losses include stock volatility or true vapor pressure, temperature, vapor-space expansion-contraction, and liquid-vapor mass transfer governed by geometry as well as vapor-space conditions

[44].

In this study, the conical vessel in Figure 4(a) generally showed the highest retained volume for each fluid. In contrast, the spherical vessel (Figure 4(d)) frequently showed the lowest retained volume (*i.e.*, the largest shrinkage). This aligns with the earlier description of the void space. As observed, the conical configuration tends to create a smaller effective headspace near the opening (and a more constrained vapor pathway). In the spherical vessel, more vapor space above the liquid can increase losses.

Both alcohols in Figure 5 and Figure 6 show a progressive, nearly monotonic decline in volume over the 7 days, with geometric separation emerging after the early days. The conical vessel retains the most, while the spherical vessel exhibits the greatest loss. This pattern is consistent with evaporation that is driven by volatility and is amplified when the vapor space can warm, cool, and renew more readily (breathing-type behavior), and reduced when the vapor space is effectively constrained.

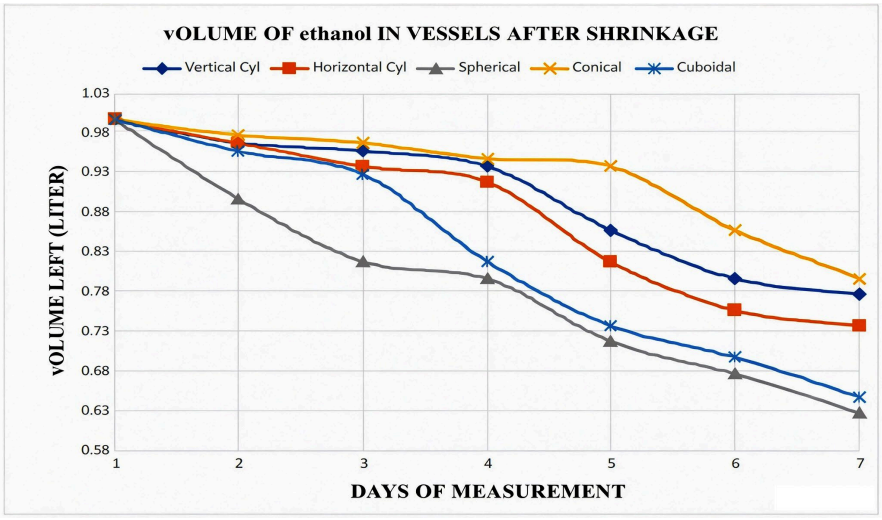


Figure 5. Shrinkage progression of ethanol in different vessel designs.

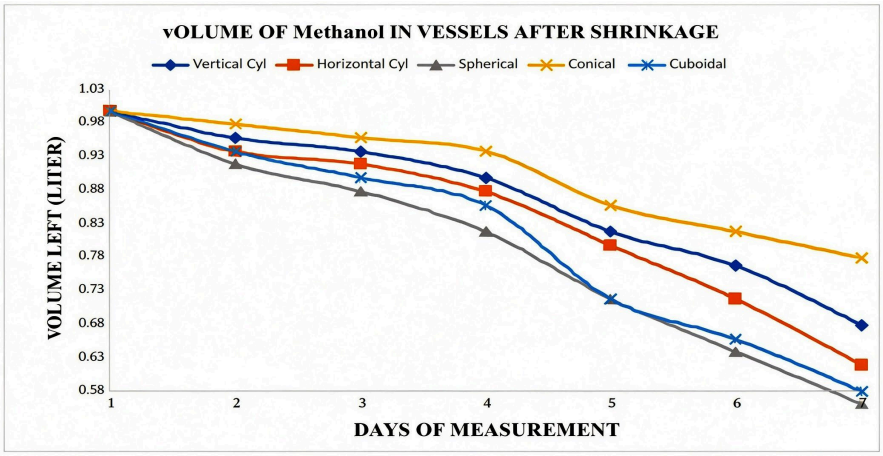


Figure 6. Shrinkage progression of methanol in different vessel designs.

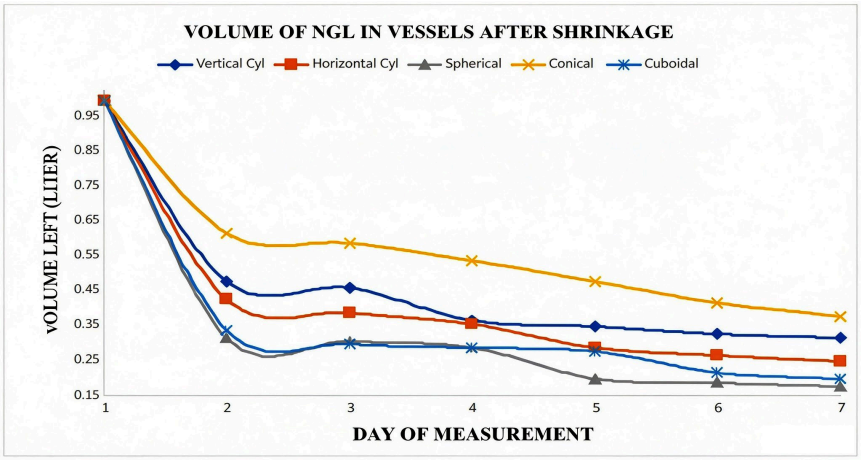


**Figure 7.** Shrinkage progression of NGL in different vessel designs.

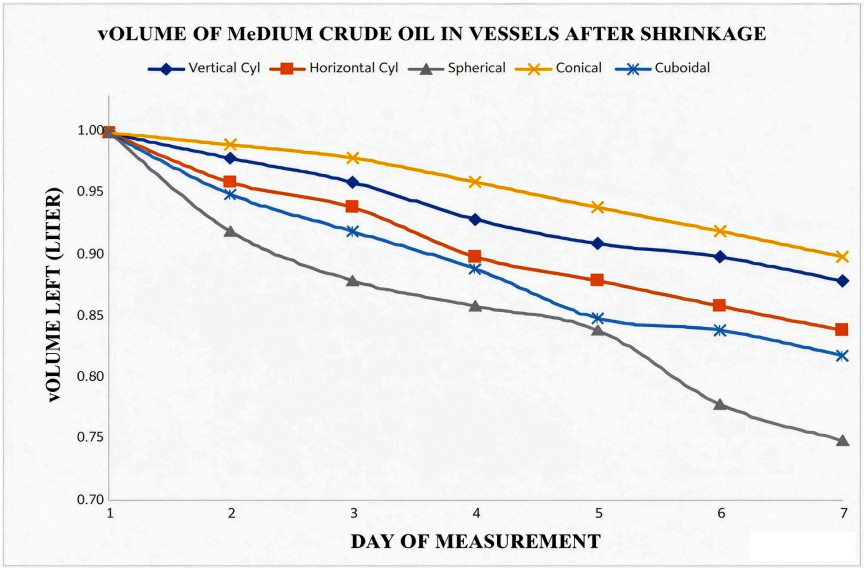


**Figure 8.** Shrinkage progression of MWC in different vessel designs.

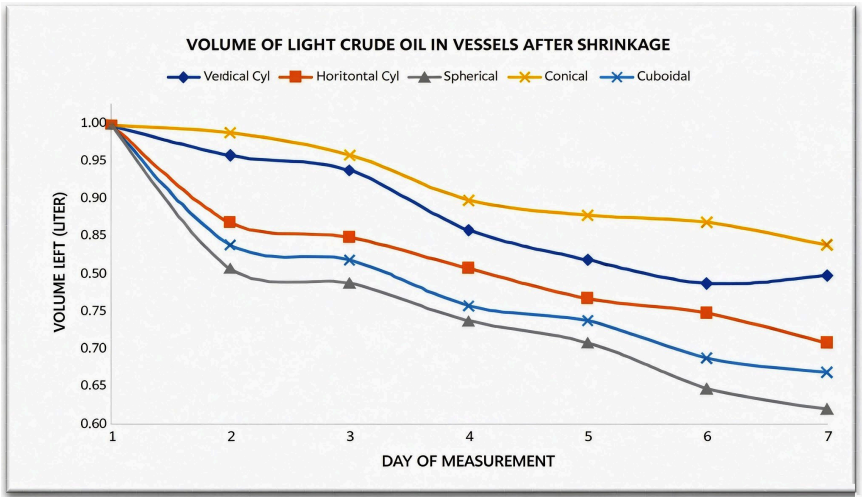


**Figure 9.** Shrinkage progression of LWC in different vessel designs.

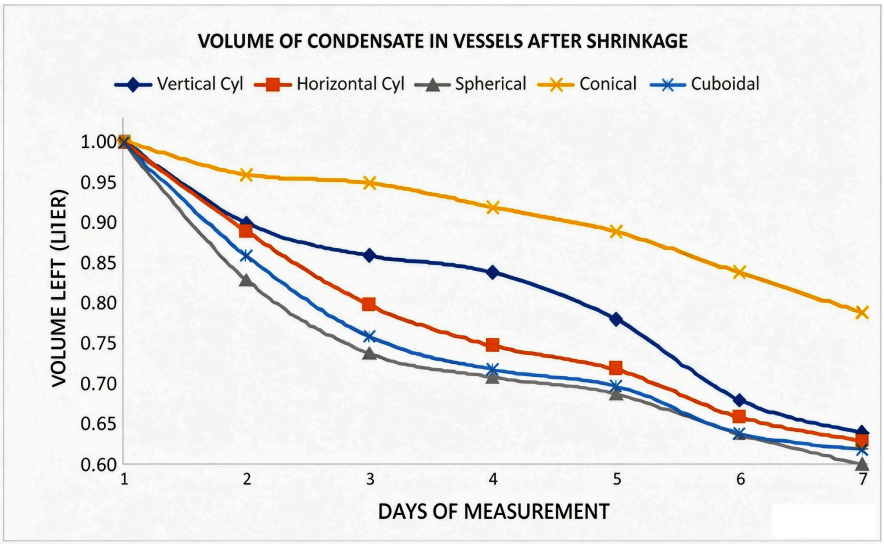


**Figure 10.** Shrinkage progression of NGC in different vessel designs.

Natural gas liquid (NGL) in **Figure 7** shows the most distinctive behaviour: a very steep Day 1→Day 2 drop in all vessels, followed by a slower decline/near-plateau for several geometries. This is characteristic of a highly volatile mixture that rapidly flashes early, then the remaining liquid becomes relatively less volatile, reducing the loss rate. Geometry effects remain strong, as the conical vessel consistently retains more; this is shown by its reduced effective vapor exchange and reduced mass-transfer driving conditions.

Natural gas condensate (NGC) in **Figure 10** exhibits a strong early decline (though generally less extreme than NGL), and then a continued geometry-dependent decrease. Here, the conical vessel also maintained the highest retained volume through Day 7, indicating that void-space limitation and reduced vapor renewal can reduce losses for volatile hydrocarbon liquids. In accordance with AP-42, standing and working losses are treated as functions of temperature-linked vapor-space behavior and stock volatility, in the sensitivity of NGC to vessel geometry [44].

The volatility of low-weight crude oil, as shown in **Figure 9**, indicates moderate shrinkage relative to alcohols, NGL, and NGC, reflecting its lower volatility. However, vessel geometry still governs ranking; the conical vessel retains the most, and the spherical vessel loses more.

This supports the interpretation that even when volatility is lower, the availability of vapor space and effective interfacial mass transfer remain important determinants of the cumulative loss observed over multi-day storage.

The medium weight crude oil (MWC) shows the smallest overall decline among the six fluids and a comparatively tighter clustering of curves. This may be due to lower volatility and the likelihood of the formation of wax-structure effects at the WAT or below; this can increase apparent viscosity, suppress free-surface convection, and reduce effective mass-transfer rates. Waxy oils are known to be rheologically complex and exhibit flow behaviours that are dependent on structure as well as thermal and shear histories, which provides a mechanistic basis for why MWC

can display lower shrinkage sensitivity than the more volatile Newtonian fluids.

### 4.5. Observable Wax-Crystallization Effects on Shrinkage Behavior

Table 1 shows that only the medium-weight crude oil (MWC) has a measurable wax appearance temperature (WAT = 31.50˚C) within the measurable range of temperatures. In contrast, methanol, ethanol, low-weight crude oil (LWC), natural gas condensate (NGC), and natural gas liquids (NGL) did not show detectable WAT under the stated condition (*i.e.*, no wax-crystallization onset above 0˚C was detected within the applied DSC protocol). WAT is interpreted as the onset of wax-crystal formation during controlled cooling, commonly identified from the first crystallization event on the DSC heat-flow trace.

Because the shrinkage experiments were performed at 25˚C - 33˚C, MWC was at or near (and partly below) its WAT, so wax crystals would be expected to nucleate and form a structure during storage. In waxy oils, such crystallization can generate a temperature- and history-dependent microstructure that produces shear-dependent viscosity, yield-like behavior, and gelation, and these effects strengthen as temperature decreases. This provides a mechanistic basis for why the MWC shrinkage curves (Figure 8) appear more gradual and less "flash-loss dominated" than highly volatile Newtonian liquids (notably NGL and NGC in Figure 7 and Figure 10).

This work was carried out at an observable temperature (25˚C - 33˚C). This could explain why the five liquids (ethanol, methanol, NGL, NGC, and LWC) did not form wax. The variation in temperature below 25˚C, at which the other five liquids may form wax, could justify comparing their evaporative shrinkage potential with the wax appearance temperature of 31.50˚C for MWC.

For wax-free fluids (MetOH, EtOH, LWC, NGC, NGL), differences in geometry that give rise to headspace or void volume and vapor exchange remain the dominant differentiator of shrinkage trajectories (Figures 5-7, Figure 9, Figure 10). For MWC, wax crystallization near the storage temperature might have contributed to the following: reduction of effective mass-transfer rates due to increased viscosity and suppressed surface convection, and increased wall wetting retention. These factors might have enabled apparent shrinkage to be more sensitive to the wetted area during discharge. The behaviors are consistent with the modern waxy-oil rheology literature on wax-crystal networks, gelation, and the strong dependence on thermal and shear history [37] [45].

## 5. Conclusions

This study compared short-term and bench-scale storage for the apparent shrinkage behavior of six fluids in five geometrically distinct vessels and linked the observed retention patterns to rheological class, wax behavior, and vessel-controlled vapor-space conditions. Differential scanning calorimetry showed that only the medium-weight crude oil (MWC) exhibited a measurable wax appearance tem-

perature, while no wax-crystallization onset was detected above 0.00˚C for methanol, ethanol, low-weight crude oil, natural gas condensate, and natural gas liquid under the DSC protocol used. Steady-shear rheometry further showed that, except for MWC, the other liquids behaved as Newtonian fluids within the tested shear-rate range, whereas MWC showed non-Newtonian, shear-thinning behavior.

The investigation on storage showed that vessel design influences apparent volume retention. It was deduced that the conical vessel retained more liquids, while the spherical vessel lost more liquid to shrinkage, indicating that vessel shape affects loss behavior through differences in exposed surface evolution, headspace development, and the renewal of vapors. The more volatile liquids, NGL and NGC, had a more evaporative shrinkage effect on vessel geometry, which showed strong early losses. By contrast, MWC displayed the smallest overall decline, possibly attributable to its lower volatility and possible wax structuring near its WAT.

The findings show that volatility is not the sole consideration for fluid shrinkage during storage. Besides volatility, interactions among fluid type, rheological state, wax tendency, and vessel geometry are also very important for a comprehensive evaluation. The results, therefore, support vessel selection and headspace control as practical strategies for minimizing short-term storage losses.

## Acknowledgements

The authors are thankful to the Department of Pure and Industrial Chemistry, the School of Science Laboratory and Technology, and Ideal Geochem and Environmental Services Limited for providing laboratory support and assistance with sampling during this study.

## Author Contributions

Conceptualization, I.E.E. and G.M.E.; methodology, G.M.E. and I.O.; software, I.E.E., P.A., G.M.E. and I. O.; validation, O.A.; formal analysis, I.E.E., G.M.E. and I.O.; investigation, I.E.E., P.A. and G.M.E.; resources, I.E.E. and G.M.E. and P.A.; data curation, O.A. and I.E.E.; Writing—original draft preparation, I.E.E. and I.O.; writing-review and editing, I.E.E. and O.A.; visualization, P.A. and O.A.; supervision, O.A.; funding acquisition, I.E.E. and G.M.E. All authors have read and agreed to the published version of this manuscript.

## Conflicts of Interest

The authors declare no conflicts of interest regarding the publication of this paper.

## References

[1] Application Viscosity (2021) Viscosity Program. https://megavpnqcrh.netlify.app/umphress88125gi/viscosity-program-951.html

[2] Tawalbeh, M., Shomope, I. and Al-Othman, A. (2024) Comprehensive Review on non-Newtonian Nanofluids, Preparation, Characterization, and Applications. *International Journal of Thermofluids*, **22**, Article 100705. https://doi.org/10.1016/j.ijft.2024.100705

[3] Lynch, S., Nama, N. and Figueroa, C.A. (2022) Effects of Non-Newtonian Viscosity on Arterial and Venous Flow and Transport. *Scientific Reports*, **12**, Article No. 20568. https://doi.org/10.1038/s41598-022-19867-1

[4] Wei, M., Lin, K. and Sun, L. (2022) Shear Thickening Fluids and Their Applications. *Materials & Design*, **216**, Article 110570. https://doi.org/10.1016/j.matdes.2022.110570

[5] Banerjee, R. and Ray, S.S. (2023) Role of Rheology in Morphology Development and Advanced Processing of Thermoplastic Polymer Materials: A Review. *ACS Omega*, **8**, 27969-28001. https://doi.org/10.1021/acsomega.3c03310

[6] Martínez-Padilla, L.P. (2023) Rheology of Liquid Foods under Shear Flow Conditions: Recently Used Models. *Journal of Texture Studies*, **55**, e12802. https://doi.org/10.1111/jtxs.12802

[7] Guo, L., Han, X., Lei, Y., Wang, L. and Yu, P. (2022) Research on Nonlinear Rheological Properties of Waxy Crude Oil Based on Large Amplitude Oscillatory Shearing. *Journal of Petroleum Science and Engineering*, **213**, Article 110444. https://doi.org/10.1016/j.petrol.2022.110444

[8] Batic, I. (2023) Reduction of Evaporation Losses in Oil and Oil Derivatives Storage Tanks: A Case Study for Warehouse in Pozega, Serbia. *Thermal Science*, **27**, 2455-2464. https://doi.org/10.2298/tsci220923172b

[9] Glushkov, S. and Valeev, A. (2023) Analysis of Methods for Accounting for the Amount of Evaporation of Petroleum Products from the Tank. *Liquid and Gaseous Energy Resources*, **3**, 59-66. https://doi.org/10.21595/lger.2023.23585

[10] Ratnakar, R.K., Pandian, S., Mary, H. and Choksi, H. (2025) Flow Assurance Methods for Transporting Heavy and Waxy Crude Oils via Pipelines without Chemical Additive Intervention. *Petroleum Research*, **10**, 204-215. https://doi.org/10.1016/j.ptlrs.2024.07.005

[11] Wu, X., Chen, Q. and He, R. (2024) Experimental Research and Estimation Model of Gasoline Evaporative Emissions from Vehicles in China. *Science of The Total Environment*, **927**, Article ID: 171875. https://doi.org/10.1016/j.scitotenv.2024.171875

[12] Shah, M.M. (2025) Calculation of Evaporation of Chemicals into Air. *Chemical Engineering Science*, **316**, Article 121937. https://doi.org/10.1016/j.ces.2025.121937

[13] U.S. Environmental Protection Agency (2024) AP-42: Compilation of Air Emissions Factors, Chapter 7.1—Organic Liquid Storage Tanks (Final Methodology Update). https://www.epa.gov/system/files/documents/2024-10/c7s1_2024final_rlso.pdf

[14] American Petroleum Institute (2016) Petroleum Measurement Standards: Chapter 19, Evaporation Loss Measurement (Catalog Listing). API Publications Catalog. https://www.api.org/~/media/files/publications/2018_catalog/2018_pubs_catalog_final_pm.pdf

[15] AMETEK Brookfield (2021) RSX Rheometer—Operation Instructions (M21-245 Rev. A), AMETEK Brookfield. https://www.brookfieldengineering.com/resourcelibrary

[16] ASTM International (2020) Standard Test Methods for Rheological Properties of Non-Newtonian Materials by Rotational (Brookfield-Type) Viscometer (ASTM D2196-20) West Conshohocken. ASTM International.

[17] International Organization for Standardization (2021) ISO 3219-2:2021-Rheology-Part 2: General Principles of Rotational and Oscillatory Rheometry. ISO.

[18] Agwu, O.E., Akpabio, J.U., Ekpenyong, M.E., Inyang, U.G., Asuquo, D.E., Eyoh, I.J., *et al.* (2021) A Critical Review of Drilling Mud Rheological Models. *Journal of Petro-*

*leum Science and Engineering*, **203**, Article 108659.
https://doi.org/10.1016/j.petrol.2021.108659

[19] Taheri-Shakib, J., Shekarifard, A., Kazemzadeh, E., Naderi, H. and Rajabi-Kochi, M. (2020) Characterization of the Wax Precipitation in Iranian Crude Oil Based on Wax Appearance Temperature (WAT): The Influence of Ultrasonic Waves. *Journal of Molecular Structure*, **1202**, Article 127239.
https://doi.org/10.1016/j.molstruc.2019.127239

[20] Yao, B., Zhao, D., Zhang, Z. and Huang, C. (2021) Safety Study on Wax Deposition in Crude Oil Pipeline. *Processes*, **9**, Article 1572. https://doi.org/10.3390/pr9091572

[21] PerkinElmer (2021) Wax Appearance Temperature Detection by DSC.
https://www.perkinelmer.com/library/app-wax-appearance-temperature-detection-by-dsc.html

[22] Cao, L., Sun, J., Liu, J. and Liu, J. (2022) Experiment and Application of Wax Deposition in Dabei Deep Condensate Gas Wells with High Pressure. *Energies*, **15**, Article 6200. https://doi.org/10.3390/en15176200

[23] Kiyingi, W., Guo, J., Xiong, R., Su, L., Yang, X. and Zhang, S. (2022) Crude Oil Wax: A Review on Formation, Experimentation, Prediction, and Remediation Techniques. *Petroleum Science*, **19**, 2343-2357. https://doi.org/10.1016/j.petsci.2022.08.008

[24] Kiyingi, W., Guo, J., Xiong, R., Zhang, S. and Gao, C. (2025) A Potentially Fast Approach for Detecting Wax Appearance Temperature and Quantification in Crude Oils Using Optical Back Scattering Analysis. *Colloids and Surfaces A*: *Physicochemical and Engineering Aspects*, **713**, Article 136517.
https://doi.org/10.1016/j.colsurfa.2025.136517

[25] Outlaw, J. and Ye, P. (2021) Wax Appearance Temperature Detection by DSC (Application Note 169686). PerkinElmer Inc.

[26] American Petroleum Institute (2020) API Standard 650: Welded Tanks for Oil Storage. 13th Edition, American Petroleum Institute.

[27] American Society of Civil Engineers (2022) Minimum Design Loads and Associated Criteria for Buildings and Other Structures (ASCE/SEI 7-22). American Society of Civil Engineers.

[28] Fallah Daryavarsari, S. and Nascimbene, R. (2024) Assessment of Steel Storage Tank Thickness Obtained from the API 650 Design Procedure through Nonlinear Dynamic Analysis, Accounting for Large Deformation Effects. *Materials*, **18**, Article 66.
https://doi.org/10.3390/ma18010066

[29] Autodesk (2024) What's New in AutoCAD 202, Autodesk Help.
https://help.autodesk.com/view/ACD/2024/ENU/

[30] García-G, D., Barco-Burgos, J., Chaparro, J., Eicker, U., Cárdenas D.R, J. and Saldaña-Robles, A. (2024) Analyzing Joint Efficiency in Storage Tanks: A Comparative Study of API 650 Standard and API 579 Using Finite Element Analysis for Enhanced Reliability. *International Journal of Pressure Vessels and Piping*, **207**, Article 105113.
https://doi.org/10.1016/j.ijpvp.2023.105113

[31] American Petroleum Institute (2021) Manual of Petroleum Measurement Standards (MPMS), Chapter 3.1A: Standard Practice for the Manual Gauging of Petroleum and Petroleum Products (Consolidated Version of 3rd Edition, Incorporating Errata 1).

[32] International Organization for Standardization (2022) ISO 7507-2:2022 Petroleum and Liquid Petroleum Products-Calibration of Vertical Cylindrical Tanks-Part 2: Optical-Reference-Line Method or Electro-Optical Distance-Ranging Method. 3rd Edition, ISO.

[33] Abou-Kassem, A.J., Bizhani, M. and Kuru, E. (2023) A Review of Methods Used for Rheological Characterization of Yield-Power-Law (YPL) Fluids and Their Impact on the Assessment of Frictional Pressure Loss in Pipe Flow. *Geoenergy Science and Engineering*, **229**, Article 212050. https://doi.org/10.1016/j.geoen.2023.212050

[34] de Rosso, N., Andrade, D.E.V. and Negrão, C.O.R. (2025) Experimental Analysis of Waxy Crude Oil Startup Flow in Pipelines. *Journal of Pipeline Science and Engineering*, Article 100251. In Press. https://doi.org/10.1016/j.jpse.2024.100251

[35] N, K., Premnath, K., D, V., Nayak, S. and S, S. (2025) Laboratory Simulation Studies on Evaporative Fuel Loss from Storage Tanks. *BIO Web of Conferences*, **172**, Article 01004. https://doi.org/10.1051/bioconf/202517201004

[36] Zhang, J., Guo, L., Gao, X. and Shi, C. (2025) Microscopic Mechanism of Wax Precipitation and Gelation of Waxy Crude Oil Based on Molecular Dynamics Simulation. *Journal of Pipeline Science and Engineering*, **6**, Article 100311.

[37] Ansari, S., Rashid, M.A.I., Waghmare, P.R. and Nobes, D.S. (2020) Measurement of the Flow Behavior Index of Newtonian and Shear-Thinning Fluids via Analysis of the Flow Velocity Characteristics in a Mini-Channel. *SN Applied Sciences*, **2**, Article No. 1787. https://doi.org/10.1007/s42452-020-03561-w

[38] Pérez-Salas, K.Y., García-Romero, E.L., Barrientos-Cruz, A.A., González-Rivera, A.S., Córdova-Aguilar, M.S., Ascanio, G., *et al.* (2026) Introducing the Concept of Yield Stress in Fluids for Students of Chemistry, Materials Science and Chemical Engineering. *Journal of Chemical Education*, **103**, 1421-1429. https://doi.org/10.1021/acs.jchemed.5c01570

[39] Rahmani, H. and Taghavi, S.M. (2026) Yield Stress Fluids in Microfluidics: Research, Applications and Opportunities. *Lab on a Chip*, **26**, 3916-3949. https://doi.org/10.1039/d5lc00864f

[40] Franco, S., Ruzicka, B. and Angelini, R. (2025) Soft and Responsive: Rheological Insights into PNIPAM Based Microgels and Applications. *Journal of Physics*: *Condensed Matter*, **37**, Article 243001. https://doi.org/10.1088/1361-648x/adbb9a

[41] Guo, L., Zhang, J., Wang, L., Chen, R. and Liu, B. (2025) Microscopic Observation of Wax Crystal Network Formation and Shear-Induced Disruption in Gelled Crude Oil. *Colloids and Surfaces A*: *Physicochemical and Engineering Aspects*, **726**, Article 137939. https://doi.org/10.1016/j.colsurfa.2025.137939

[42] Environmental Protection Agency (EPA) (2024) Final Revisions to AP-42 Chapter7, Section 1: Organic Liquid Storage Tanks. https://www.epa.gov/air-emissions-factors-and-quantification/final-revisions-ap-42-chapter-7-section-1-organic-liquid

[43] Romagnuolo, L., Frosina, E., Andreozzi, A., Senatore, A. and Fortunato, F. (2021) Experimental Analysis of Evaporative Emissions of Ethanol-Blended Gasoline in Automotive Tanks at Different Temperature Conditions. *Fuel*, **304**, Article 121427. https://doi.org/10.1016/j.fuel.2021.121427

[44] Environmental Protection Agency (EPA) (2021) AP-42: Compilation of Air Pollutant Emission Factors (5th Edition, Vol. I), Chapter 7-Liquid Storage Tanks, Section 7.1-Organic Liquid Storage Tanks.

[45] Andrade, D.E.V. and Negrão, C.O.R. (2025) Rheology of Waxy Oils: A Critical Review. *Applications in Engineering Science*, **21**, Article 100202. https://doi.org/10.1016/j.apples.2024.100202